Solar Physics
DOI: 10.1007/•••••-•••-•••-••••-•

Solar Radio Imaging at Arecibo: The Brightness Temperature and Magnetic Field of Active Regions

Periasamy K. Manoharan[1]•• · Christopher J. Salter[1] · Stephen M. White[2] · Phil Perillat[3] · Felix Fernandez[3] · Ben Perera[1] · Arun Venkataraman[3] · Christiano Brum[1]

Abstract

Strong solar magnetic fields are the energy source of intense flares and energetic coronal mass ejections of space weather importance. The key issue is the difficulty in predicting the occurrence time and location of strong solar eruptions, those leading to high impact space weather disturbances at the near-Earth environment. Here, we report regular solar mapping made at X-band (8.1 – 9.2 GHz) with the Arecibo 12-m radio telescope. This has demonstrated its potential for identifying active regions, about one half to a day in advance, when they rotate on to the central meridian of the Sun, and predicting the strongest flares

✉ P. K. Manoharan
mano.rac@gmail.com

C. J. Salter
csalter@naic.edu

S. M. White
stephen.white.24@spaceforce.mil

P. Perillat
phil@naic.edu

F. Fernandez
felix.omar.fernandez@gmail.com

B. Perera
bhakthiperera@gmail.com

A. Venkataraman
arun@naic.edu

C. Brum
cbrum@naic.edu

[1] Arecibo Observatory, University of Central Florida, Puerto Rico 00612, USA.

[2] Space Vehicles Directorate, Air Force Research Laboratory, Albuquerque, NM, USA.

[3] Arecibo Observatory, Yang Enterprises Inc., Arecibo, Puerto Rico 00612, USA

and coronal mass ejections directed towards the Earth. Results show (i) a good correlation between the temporal evolution of brightness temperature of active regions and their magnetic configurations; (ii) the ability of the mapping data to provide a better picture of the formation sites of active regions and to accurately track their evolution across the solar disk, giving forewarning of intense solar eruptions leading to severe space weather consequences; (iii) the importance of long-term monitoring of the Sun at X-band for understanding the complex three-dimensional evolution of solar features as a function of solar activity. The key point in this study is the identification of the magnetic properties of active regions on the solar disk to aid in improving forecast strategies for extreme space-weather events.

Keywords: Active Regions, Magnetic Fields, Structure; Chromosphere; Coronal Mass Ejections; Flares, Relation to Magnetic Field; Radio Emission, Active Regions; Solar Cycle, Observations; Space Weather

1. Introduction

Solar magnetic fields play a critical role in a wide variety of phenomena occurring on the Sun, ranging from slowly evolving structures such as coronal holes, sunspots, and coronal loops, to highly dynamical phenomena such as the acceleration of the solar wind, acceleration of charged particles, solar flares, and coronal mass ejections (CMEs). The magnetic field in the solar atmosphere essentially controls the plasma structure, storage of free magnetic energy, and its release at times of flares and/or mass ejections (e.g., Fleishman et al. 2022). The areas of strong magnetic field concentration on the surface of the Sun form active regions, which are embedded in groups of sunspots of the same magnetic polarity, followed by groups of sunspots of opposite polarity. Specifically, active regions coupled to sunspot groups of complex polarity of γ or γ-δ configuration, as per the Hale or Mount Wilson scheme (e.g., Hale et al. 1919; Künzel 1965), are prone to produce significantly intense flares and CMEs. However, such spots are limited in number to $<$1% of the total number of spots compared to the numerous β spots of bipolar characteristic, which produce flares of lower intensity (e.g., Jaeggli and Norton 2016). Therefore, the key issue is to predict the occurrence time and location of strong solar eruptions, *i.e.*, those leading to the high impact space weather disturbances in the near-Earth environment.

The solar magnetic fields are observed directly at the photospheric level, whereas direct field measurements are very difficult in the dynamic corona due to its low density. The inference of the coronal field is largely via data-driven models, which are limited by the basic assumption that the coronal magnetic field remains in static equilibrium. However, the X-ray and extreme ultraviolet (EUV) emissions from the optically-thin corona above an active region, originating at the top of the complex magnetic field network, relate to the inhomogeneous, hot, and dense plasma and they provide a remarkable view of the magnetic activity above the active region (Krucker et al. 2008). In a close resemblance, but in the extended solar atmosphere, the radio opacity decreases with increasing observing frequency and the effective radio emission height, from meter to

centimeter wavelengths, moves from the corona to the chromospheric region. The radio signatures of an active region in the frequency range of 5 – 10 GHz provide a powerful diagnostic of the gyro-synchrotron radiation from high-energy electrons trapped in small-scale magnetic field loops and the observed bright features are gyro-resonance emitting regions where the field strength exceeds 600 G (e.g., Bastian, Benz, and Gary 1998; White 1999; Shibasaki, Alissandrakis, and Pohjolainen 2011; Nindos 2020).

Typically, the gyro-resonance spectrum peaks in the frequency range of 5 – 10 GHz and provides an *indirect* measure of magnetic fields above the photosphere (Gary et al. 2018). Moreover, observations in this frequency range do not wholly resemble those at the soft X-ray and/or EUV bands, but they do largely imitate the photospheric magnetograms (Dabrowski and Benz 2009; Nita, Gary, and Lee 2004; White et al. 2011). Since the magnetic complexity of an active region crucially determines the occurrence of intense flares and energetic CMEs (Priest and Forbes 2002; Yashiro et al. 2005), the present study emphasizes the importance of regular mapping of the Sun at ∼8.1 – 9.2 GHz in revealing the magnetic characteristics of eruptive regions analogous to the magnetogram data.

In Section 2 of this paper, we provide a brief description of the Arecibo 12-m radio telescope. In the following sections, we discuss our X-band (8.1 – 9.2 GHz) solar mapping observations and report significant results on, (i) tracking the formation and evolution of active regions leading to strong solar eruptions of space weather importance, (ii) understanding the relationship between the radio emission brightness and the magnetic field properties of the quiet Sun and flaring regions, (iii) the global view of the solar features over several solar rotations, and (iv) the "solar flux density – brightness temperature" relationship. Finally we give the concluding remarks in Section 8.

Figure 1. The hill-top view of the Arecibo 12-m Radio Telescope.

Table 1. Antenna Location and Parameters

Site location	
– Longitude	66° 45′ W
– Latitude	18° 20′ N
– Elevation (above MSL)	496 m
Cassegrain focus, F/D ratio (primary surface)	0.375
Surface accuracy (includes fabrication accuracy and effects of wind, gravity, and temperature)	0.38 mm (RMS)
Possible frequency range	2.1 – 32 GHz
Pointing accuracy (at wind speed $\lesssim$50 km per hour)	$\sim$30 arcsec
Elevation range	+5 to 88 deg
Azimuth range	-180 to 360 deg
Slew and scan rates	
– Azimuth	up to $\sim$5 deg/s
– Elevation	up to $\sim$1 deg/s

Table 2. System Performance

System parameters	X-band
Frequency range	8.1 – 9.2 GHz
HPBW[@]	$\sim$10 arcmin
T_{sys}*	123 K
SEFD*	4200 Jy

[@]HPBW is the telescope′s half-power beam width
*T_{sys} and SEFD vary with elevation (see Figure 2)

2. The Arecibo 12-m Radio Telescope

The Arecibo Observatory operates a 12-m diameter parabolic reflector radio telescope. It was manufactured by Patriot Antennas Inc, Albion, Michigan, USA. The 12-m telescope was installed in 2011 on a hill-top within the observatory campus. It is a fully steerable alt-azimuth-mount telescope with a primary focal length to diameter ratio of 0.375. The telescope can cover an elevation range of $\sim$5° – 88° and provides a coverage in declination, between $\sim -65°$ and +90°. The hill-top view of the 12-m telescope is shown in Figure 1. The geographic coordinates of the telescope site and the mechanical specifications of the antenna are given in Table 1.

2.1. The Room-temperature Receiver Systems

The 12-m radio telescope operated with room-temperature receiver systems until 10 April 2023, which covered the frequency ranges of 2.21 – 2.34 GHz (S-band) and 8.1 – 9.2 GHz (X-band) and recorded dual polarization signals using the FPGA-based Mock Spectrometer, which contains seven boxes and

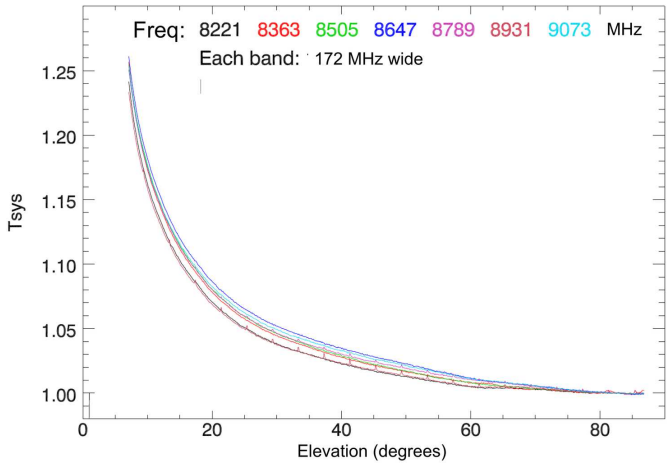

Figure 2. The variation of the 12-m radio telescope's system temperature (T_{sys}) as a function of elevation angle at X-band. Seven frequency bands, each of 172-MHz bandwidth, are shown in different colors. Each band's T_{sys} is normalized to its average value of 123 K at elevations of ∼80-85 degrees (see Table 2).

each box handles bandwidth up to 172 MHz (http://www.naic.edu/~astro/mock.shtml). The 12-m telescope takes advantage of RFI protection from the Puerto Rico Coordination Zone (PRCZ) at frequencies below 15 GHz, which covers Puerto Rico and nearby Puerto Rican islands. (https://www.naic.edu/ao/scientist-user-portal/science-tools/pr-coordination-zone). As a stand-alone telescope, the observing time of the 12-m antenna is mostly shared among the mapping of the Sun at the X-band (e.g., Manoharan et al. 2022; Manoharan et al. 2023) and the monitoring of pulsars and FRBs at the S-band (e.g., Perera et al. 2022; Perera et al. 2023). The observing programs of the telescope also include mapping of large angular-size continuum radio sources, monitoring of selected AGNs and blazars, spectral line studies, etc. Additionally, the 12-m telescope provides strong support for student programs, such as the NSF-funded *Research Experience for Undergraduate* (REU) and *Partnerships in Astronomy and Astrophysics Research and Education* (PAARE) programs.

The properties of the X-band room-temperature receiver are given in Table 2. The table lists the Frequency range, Half Power Beam Width (HPBW), the typical System Temperature (T_{sys}), and System Equivalent Flux Density (SEFD). It is to be noted that the system temperature (T_{sys}) varies as a function of elevation angle as shown in Figure 2, which shows each band′s T_{sys} normalized to its average value of 123 K at elevations of ∼80-85 degrees. Its average functional form at X-band is given by,

$$T_{\rm sys} = 0.9523 + 0.0477 \cdot \sin(E)^{-0.85}, \quad (1)$$

where E is the elevation angle. Correspondingly, the SEFD also varies as a function of elevation angle. The X-band, 8.1 – 9.2 GHz, is divided into seven bands of width 172 MHz, each covering a box of the Mock spectrometer. In the case of solar mapping, the system is calibrated before and after each map, by

taking 'on – off' cal (i.e., a value of ∼30 K) at a position away from the Sun. Since even the quiet Sun is strong at X-band (refer to Figures 15 and 16), the solar attenuator is needed and the uncertainty in the measured brightness temperature is rather small. However, the important point is that the performance of the X-band system can be considerably affected (i.e., attenuated) by rain (i.e., T_{sys} increases with the presence of rain, or even thick cloud coverage, along the line of sight to the radio source) and such observations are not considered in the analysis. More extensive details of performance of the system can be seen at http://www.naic.edu/~phil/hardware/12meter/sysperf.

3. Solar Radio Mapping

Solar mapping with the Arecibo 12-m Radio Telescope was initiated in mid-December 2021. 'East-west' raster scans of the Sun were taken covering a range of ±1° respectively in right ascension and declination, with respect to the center of the Sun. Each set of scans provides a calibrated map of the two-dimensional distribution of brightness temperature over the Sun. Figure 3 shows examples of full images of the Sun at 8647 MHz, a frequency close to the center of the recorded band of 8.1 – 9.2 GHz, observed on 16 May 2022 and 03 January 2023, along with the near-simultaneous EUV images of the Sun observed by the *Atmospheric Imaging Assembly* (AIA) on board the *Solar Dynamics Observatory* (SDO) in the wavelength band of 19.3 nm, and the photospheric magnetograms recorded by the *Helioseismic Magnetic Imager* (HMI) on board SDO (Pesnell, Thompson, and Chamberlin 2012; Lemen et al. 2012). The white circle plotted on the radio images indicates the size of the optical disk of the Sun.

In a day, typically 5 to 10 maps are made to monitor the evolution of the brightness temperature distribution of the Sun. Since the 12-m radio telescope covers the frequency band of 8.1 – 9.2 GHz, at a given time seven simultaneous maps are made at frequency intervals of ∼172 MHz. Inter-comparison between these maps provides a useful handle on the identification and elimination of radio frequency interference, should this be present. Each radio map represents the brightness distribution of the Sun, in a sense, the 'average' characteristics of active and quiet regions on the Sun over the scan duration of ∼30 min. However, the other space-based images compared are snapshots of the Sun with shorter exposure times.

The spatial resolution of the 12-m telescope at 8.1 – 9.2 GHz is limited to ∼10 arcmin. Nevertheless our maps provide a clear view of the emission brightness temperatures of active and quiet regions on the Sun. For example, in the radio map observed on 16 May 2022 (top row, left image; Figure 3), the presence of an active region is identified with an enhanced brightness temperature, ∼10,500 K, whereas quiet regions are at an average temperature of about 8000 K. The mid-latitude coronal hole (i.e., open magnetic field region of low density), as indicated by the low emitting region of the EUV image, is also associated with a low-brightness temperature of about $\lesssim$6000 K. Likewise the map on 03 January 2023 (bottom row, left image; Figure 3) shows the presence of three active sunspots groups, one of them located in the southern hemisphere and the others

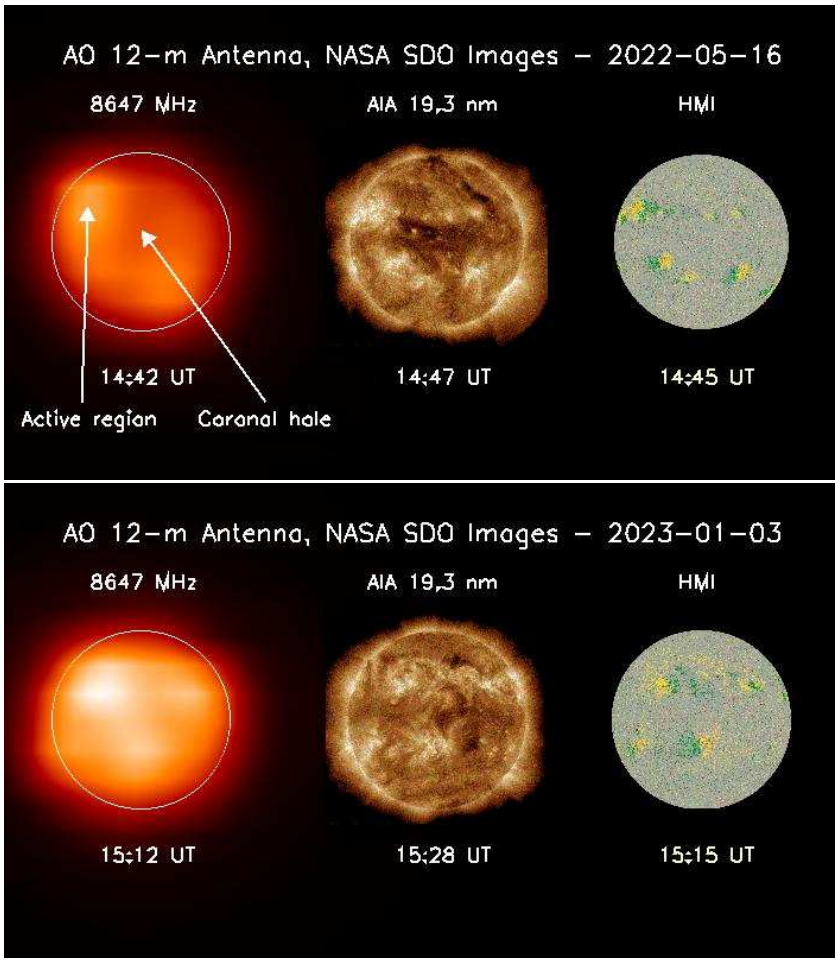

Figure 3. (Left images on the top and bottom rows) Sample images of the Sun on 16 May 2022 and 03 January 2023 at 8647 MHz made with the 12-m Arecibo telescope. The white circles on the images indicate the optical disk of the Sun. In the radio image of the top plot, a bright emitting active region and a low-emitting mid-latitude coronal hole are evident and are indicated by arrows. The bottom radio image shows three active regions, one located in the southern hemisphere, the other two in the northern hemisphere. Each radio image is compared (middle) with the near-simultaneous EUV image of the Sun at 19.3 nm and (right) the photospheric magnetogram respectively by AIA and HMI on board the NASA SDO space mission.

in the northern, in correspondence with the EUV image and the magnetogram. The brightness temperatures of these active regions lie between ∼11,000 and 13,000 K.

3.1. Peak Radio Brightness Temperature

In Figure 4, the peak brightness of the Sun (in kiloKelvin), observed with the 10-arcmin beam of the 8.6-GHz images is displayed in the top panel. This covers

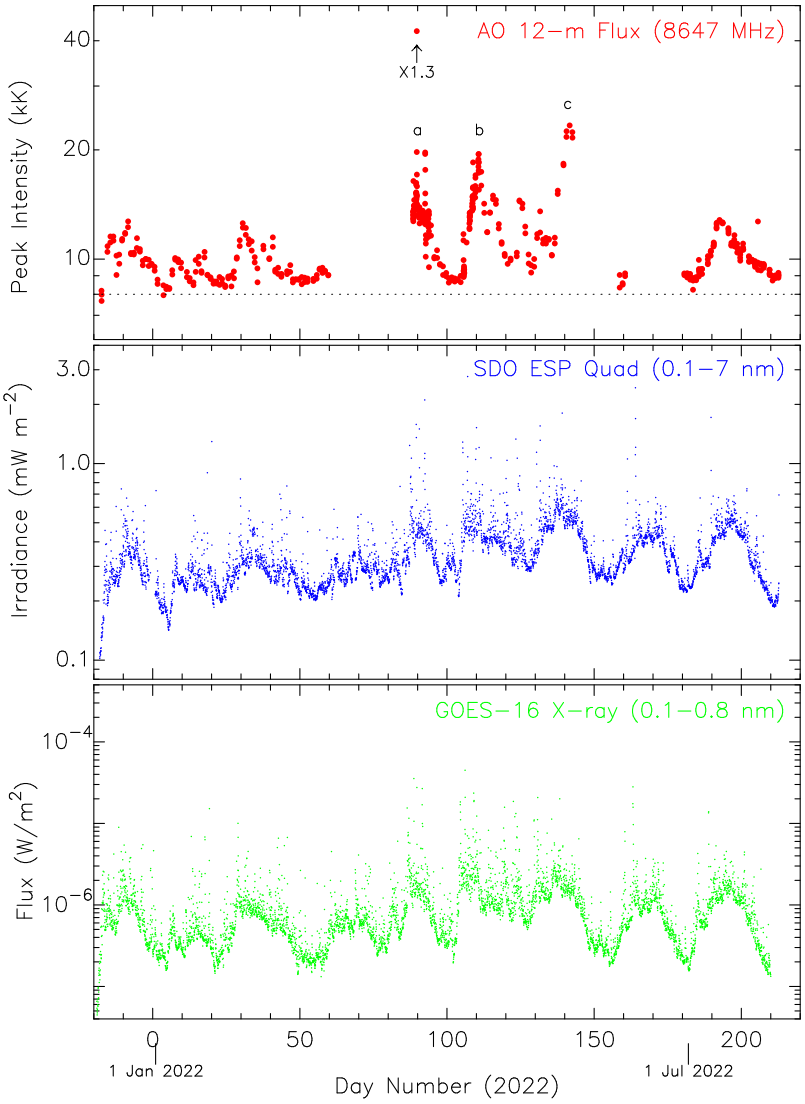

Figure 4. (Top) Peak brightness (in kiloKelvin) of the Sun at 8.6 GHz obtained from the Arecibo 12-m radio telescope plotted for dates from 13 December 2021 to 31 July 2022, in the ascending phase of the current solar cycle 25. The horizontal dotted represents the brightness temperature of the quiet Sun. Data gaps are due to the non-availability of the telescope for observation (i.e., taken for maintenance and/or upgrade works). (Middle and Bottom) Hourly average EUV (EVE/SDO) and X-ray (GOES) fluxes are plotted for comparison. The three peaks marked on the radio plot with the letters '*a*', '*b*', and '*c*' are dominant, and correspond to strong emission from magnetically-active regions of 'β-γ-δ' configuration.

the period between 13 December 2021 and 31 July 2022, which is in the onset of the ascending phase of the current solar cycle 25. The gradually building up activity of the Sun is evident in the brightness, which includes the signatures of active regions responsible for X- and M-class flares, as well as quiet days of lesser activity. In the central and bottom panels of the figure respectively, hourly-averaged EUV (0.1 – 7 nm) irradiance of the Sun observed by the *Ultraviolet Variability Experiment* (EVE) on board SDO (Woods et al. 2012) and X-ray (0.1 – 0.8 nm) flux by the NOAA *Geostationary Operational Environmental Satellite* (GOES-16) (http://www.swpc.noaa.gov/Data/goes.html) are plotted for comparison.

In the radio brightness plot, each point indicates the typical average peak brightness on the disk of the Sun and each intense peak is associated with an isolated active region on the Sun. In addition, when the mapping time coincided (or partly overlapped) with a flare, such data point recorded the brightening corresponding to the particular phase of the flare. For example, one of the maps made on day number 89 (30 March 2022) included the rising phase of the X-1.3 class flare, the first intense flare of the current solar cycle, and recorded a brightness temperature of ∼42,000 K (see top panel of Figure 4). Beside several systematic peaks, the radio brightness profile reveals the interesting result that the 8.6-GHz brightness temperature of the quiet Sun in the absence of activity, is ∼8000 K, as indicated by the dotted horizontal line in the top panel. This is likely the representative temperature of the upper chromosphere of the quiet Sun at ∼3000 km above the photosphere (e.g., Zhang, White, and Kundu 1998; Avrett and Loeser 2008).

The strong radio emission from the Sun between day numbers 90 and 140, three peaks (indicated by letters '*a*', '*b*', and '*c*' in the top panel of Figure 4) show systematic increase and decrease that are much more prominent than are seen in the EUV and X-ray fluxes. These correspond to emission from multiple-pole magnetically-active, 'β-γ-δ', regions developed on the Sun, from where intense flares and energetic CME eruptions were observed (e.g., Jaeggli and Norton 2016; Yashiro et al. 2005), and respectively correspond to active regions AR#2975, ARs#2993/2994, and AR#3014. In fact, the '*b*'-peak′s ARs#2993/2994 were the return of AR#2975, which appeared at the east limb of the Sun on 15 April 2022, and during the subsequent rotation decayed to a less active state. For each peak, when the magnetic configuration of the active region attained β-γ configuration, the brightness temperature increased to a level of ∼13,000 K. As the peak was approached, it reached ∼19,000 – 21,000 K and the magnetic configuration developed to β-γ-δ. The notable point is that all the M-class flares were produced when the brightness temperature was ≥13,000 K, whereas X-class flares occurred close to the peak of ∼20,000 K.

It is valuable to detect rarer intense flares and CMEs, with the help of the 12-m radio mapping, when an active region attains the β-δ configuration. Figure 5 shows typical examples of Arecibo radio images made at 8.6 GHz on 29 March, 24 April, and 17 May 2022, after the development of β-γ magnetic configuration, of peak brightness temperatures in the range of 13,000 – 16,000 K. Alongside each radio image is shown the same day′s complex magnetogram of the bright emitting region from the HMI on board the SDO space mission (Scherrer et al.

2012). Such an active region while crossing the central meridian of the Sun would release Earth-directed CMEs/flares, which are liable to cause severe space-weather impacts at the near-Earth space. However, the occurrence of this type of complex active region is infrequent and represented by only ∼1% of the sunspot population (e.g., Jaeggli and Norton 2016). Thus the great advantage of these measurements is that they can identify an eruptive region when it rotates close to the central meridian of the Sun, about one half to a day in advance, and predict the strongest flares and CMEs.

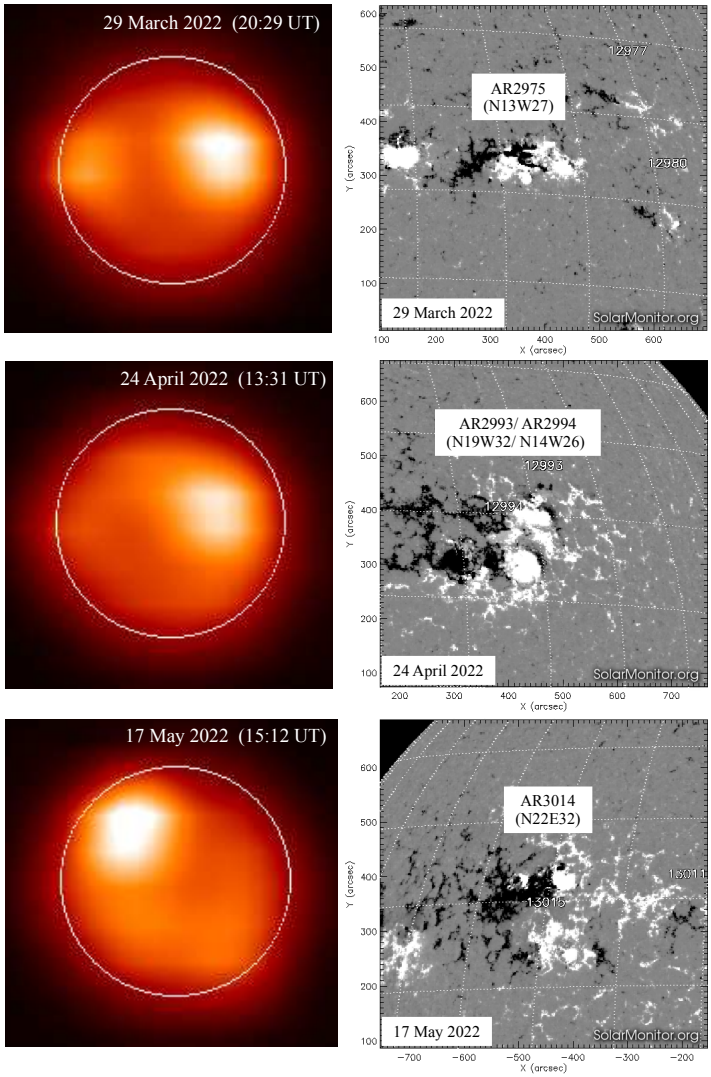

Figure 5. (Left) Arecibo radio images at 8.6 GHz from 29 March, 24 April, and 17 May 2022, with peak brightness temperatures in the range of 13,000 – 16,000 K and of magnetic configurations between β-γ and β-γ-δ. (Right) The corresponding HMI/SDO magnetograms of the bright emitting portions (courtesy of *SolarMonitor.org*).

4. Evolution of X-band Brightness Temperature

The 12-m radio telescope observations presented in this study cover the period between 13 December 2021 and 09 April 2023, which is in the ascending phase of the current solar cycle #25. The solar mapping observations were terminated at ∼18 UT on 09 April 2023 and the 12-m telescope was released to the telescope engineering team on 10 April 2023 for the installation of the wideband cooled receiver system (refer to Section 8). The regular radio mapping observations so far accomplished have been useful to (i) locate and track several active regions between their appearance at the east limb of the Sun and disappearance (i.e., rotation to the backside of the Sun) at the west limb, (ii) compare the evolution of active regions with their daily magnetic properties, such as estimated area, number of sunspots within the active group, and magnetic configurations, and (iii) study the brightness temperature evolution of the Sun as a function of the phase of the current solar cycle #25.

Several active regions crossed the solar disk without significant change, whereas a small fraction evolved from a simple magnetic configuration (e.g., α or β configuration) to complex β-δ and/or β-γ-δ configurations, and their brightness temperature profiles showed a remarkable increase to a maximum value, followed by a gradual decrease, or stayed at the increased level until they rotated off the visible disk of the Sun. In Figure 6(a) to (d), daily X-band peak-brightness temperature measurements are plotted with red dots for the active regions, #2993, #3089, #3153, and #3190, during their crossing of the solar disk. The cartoons included in Figure 6(c) depict the typical locations of the active region #3153 on the solar disk at three different epochs. In the cases of active regions, i.e., #2993, #3089, and #3153, during their passage on the solar disk, although each one of them showed an increase in brightness temperature to a peak value, followed by a gradual decrease, their temperature profiles vary in shape, width and the intensity during the rotation from the east to the west limb of the Sun. Thus, the differences in the formation, development, and decay of active regions indicate the challenges involved in predicting the intense flare/CME space-weather events and emphasize the importance of the regular monitoring of active regions, as demonstrated in the current study.

4.1. The Magnetic Configuration of Active Regions

A daily solar active region summary report is compiled and prepared based on the analysis of individual observatory reports from the Solar Optical Observing Network (SOON) by the NOAA Space Weather Prediction Center (SWPC) and US Air Force (USAF) (https://www.swpc.noaa.gov/products/solar-region-summary). The report released at the start of each day typically includes the location of an active region on the face of the Sun, its area, the number of visible sunspots within the region group, and the type of its magnetic configuration. The results of Figure 6(a) to (d) are compared with the daily magnetic properties of the active regions. For instance, close to the maximum of these brightness temperature profiles, the magnetic configurations of active regions, #2993, #3089, #3153, and #3190, developed to β-γ, β-δ-γ, β-γ, and β-δ-γ, respectively. The maximum

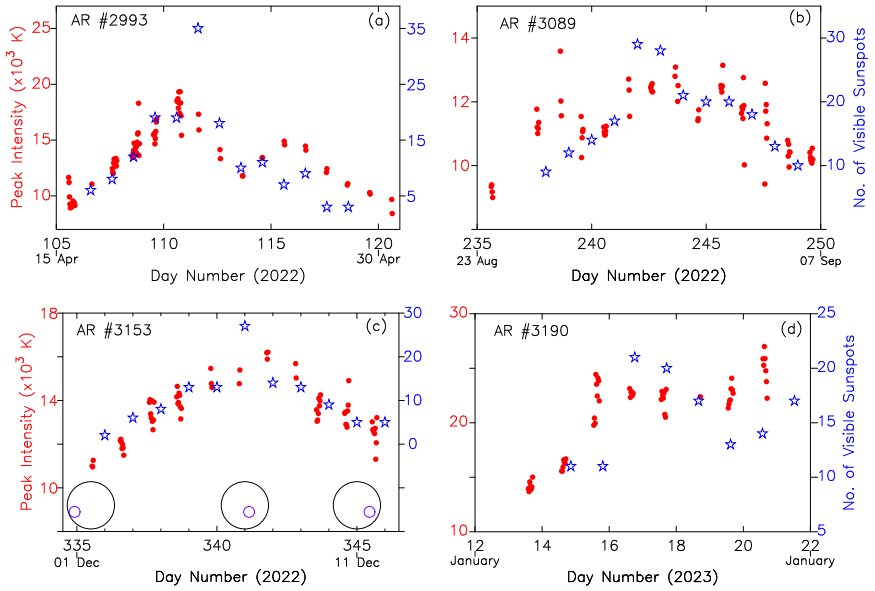

Figure 6. Plots (a) to (d) show the evolution of peak brightness temperature (in kilo Kelvin) of active regions as a function of day number. X-band brightness temperature data points (at 8.6 GHz) are plotted with red dots and the corresponding vertical axis is shown in red on the left-hand side of the plots. Daily estimates of the number of visible sunspots within each active region, obtained from NOAA SWPC, are compared with brightness temperature and plotted with blue star symbols. Its corresponding scale is shown in blue on the right-hand side vertical axis. In plot (c), the solar-disk cartoons depict the typical rotation of the AR#3153 from the east to west limb of the Sun in the southern hemisphere.

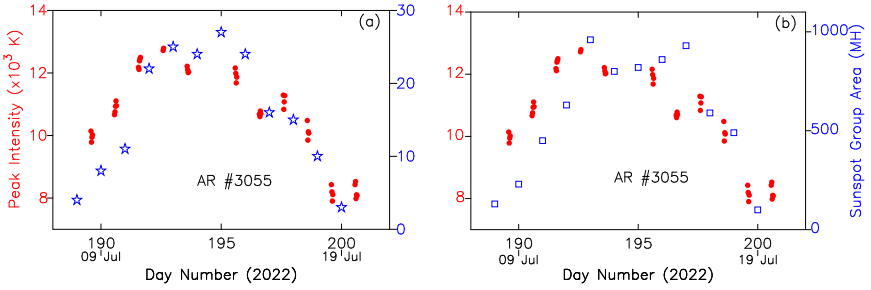

Figure 7. Plots for the AR #3055, similar in format to Figure 6, respectively compare the X-band temperature evolution with the visible number of sunspots and the area of the sunspot group in millionths of the solar hemisphere (MH) (blue square symbols).

brightness temperatures ranged from ∼16,200 to ∼27,000 K, and each active region went through different types of evolution.

Additionally in Figure 6(a) to (d), for each active region, along with the measurements of the brightness temperatures, the daily estimates of the number of visible sunspots within the active region group are plotted with blue star symbols, with the corresponding scale shown on the right side of the vertical axis of each plot. The correlation between the brightness temperature of an active

region and the development of sunspots (i.e., magnetic activity) is obvious from these plots. However, a comparison between the number of sunspots and brightness temperature near the maximum suggests a likely range of temperatures for a given number of sunspots, or vice versa. The results are further discussed in Section 5, which examines the observations of flare activity in the period between 13 December 2021 and 09 April 2023 (also refer to Figure 9).

Figure 7(a) shows the X-band temperature profile of active region #3055, which attained a maximum of ∼12800 K, which is less than the maximum values measured for the other active regions shown in Figure 6. Moreover, the magnetic configuration of this active region also evolved from the α type at the east limb of the Sun to the β type around the peak of the temperature profile, but not to a complex state. It returned again to the initial state close to the west limb, where the measured temperature was around 8000 K, which is in agreement with the long-term quiet Sun (or background) emission (see Figure 4). Similar to the temperature profile, the number count of sunspots in the region also evolves (or increases) from a count of 4 at the east limb to a maximum of 27 and then decays to a count of 3 at the west limb. In Figure 7(b), temperature measurements of the active region are compared with the area estimates of the active region, given in millionth of the solar hemisphere area (MH), available from the daily solar region summary reports (https://www.swpc.noaa.gov/products/solar-region-summary). The good agreement observed between "brightness temperature and active group area" has also been confirmed for other active regions. In the next section, we examine the relationship between the number of sunspots in an active group and its area for a large number of flaring sites located close to the central meridian of the Sun.

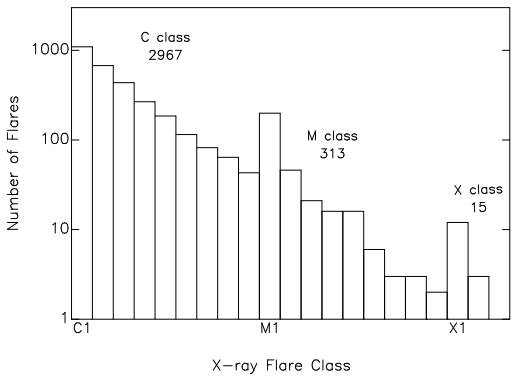

Figure 8. Distribution of the number of flares of magnitudes from C1 to X2 classifications observed during the period between 13 December 2021 and 10 April 2023. In this ascending phase of solar cycle #25 (see Figure 13), the number of flares of classifications from C1 to X2 is 3295. About 10% of these are M-class events. The X class flares represent only ∼0.5% of the population of the total number of events shown in the figure.

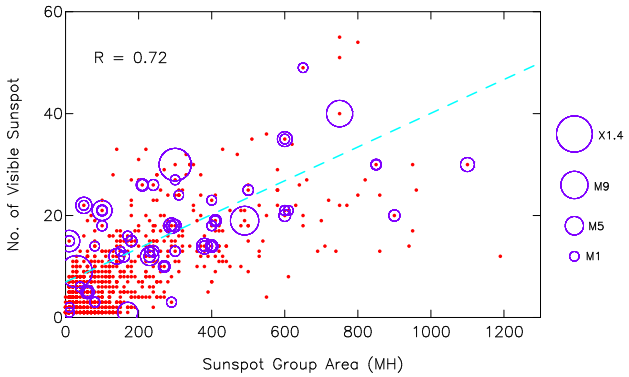

Figure 9. Scatter plot between the number of visible sunspots of flare-producing active region groups and their associated sunspot group areas. These active regions located within ∼±30° from the Sun's center produced flares of magnitude ≥C1 (see Figure 8). The number of sunspots shows an increasing trend with the area and the linear correlation coefficient is ∼0.72. However, for a given area of a group, a large scatter is seen in the number of sunspots. The active regions producing flares of M and X classes are indicated by circles, and the diameter of the circle corresponding to the magnitude of the flare.

5. The Magnetic Properties of Flare-Producing Active Regions

In continuation of the above results on the relationship between "the brightness temperature and magnetic property of active region", we also carefully examined the magnetic characteristics of moderate to intense solar flare producing regions. Flares are classified according to their X-ray intensity in the wavelength range 0.1 to 0.8 nm. The weakest flares are A- and B-class, followed by C-, M- and X-class, the increase in X-ray intensity from one class to the next being by a factor of 10, where the intensity of a C1 flare is 10^{-6} W m^{-2} and the X1 is at 10^{-4} W m^{-2}. In the current period of study, 13 December 2021 to 09 April 2023, a total number of 3295 X-ray flares of intensity C1 and above were observed, their distribution being shown in Figure 8. These flares were associated with active regions of different magnetic configurations of less evolved and simple β types to evolved and complex β-γ-δ stages. A great fraction of them, i.e., 2967 events (∼90%), are in the weak-to-moderate intensity C-class category, 313 events (∼9.5%) in the M-class, and only the 15 remaining events (≤0.5%) in the intense X1 and X2 classes. Thus, in the ascending phase of solar cycle #25, intense flares were limited to a small fraction.

In the above set of 3295 flare events, 1028 events that originated close to the central meridian of the Sun, i.e., within ±30° of the longitude and latitude of the Sun's center, have been selected. For each one of these, the magnetic properties of the flaring site are compared. Figure 9 displays the scatter plot between the number of visible sunspots in the flare region and its area, which is given in millionth of the solar hemisphere area (MH). In spite of the large scatter in the plot, there is an overall increasing trend between the number of sunspots and the area, with a correlation coefficient of +0.72. The active regions which were responsible for intense flares of M and X classes are marked with circles. The diameter of the circle indicates the flare intensity as given in the legend at

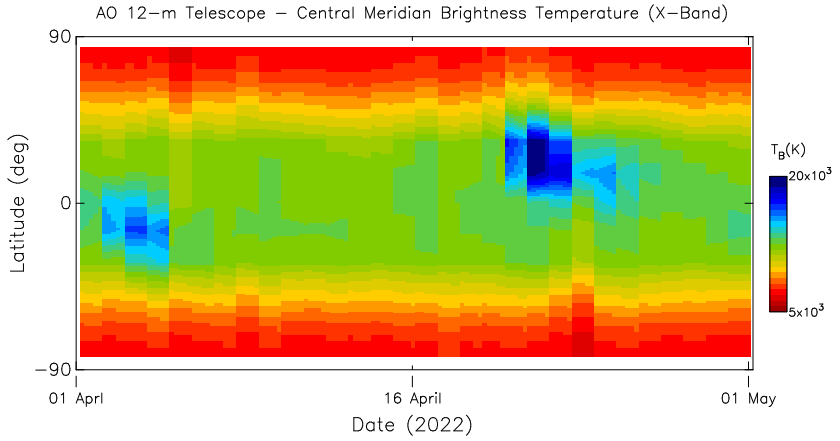

Figure 10. A synoptic map made from a sequence of central meridian cuts taken from the daily images of the 12-m telescope at 8647 MHz between 01 and 30 April 2022. It covers the full Carrington rotation #2256 and part of the end portion of rotation #2255. Two bright active regions centered respectively around 03 and 21 April 2022 are clearly seen in the brightness distribution. The sunspot belt of moderate emission occupies the ∼30° of the equatorial region. The stability of the long lived low-emitting coronal holes in the high-latitude regions are evident in the map (see Section 6).

the right-hand side of the vertical axis. An observed active region, due to its possibility of non-evolving or evolving condition, may be represented in the plot by a single point or more than one point. Moreover, on some occasions, an active region might have been the source of more than one flare of the same or varying strength, which are indicated by concentric circles on a point.

The above results of magnetic properties of flaring sites indicate that for an active region, at the time of its evolution or at the developed complex state (e.g., β-δ or β-γ-δ), it is a great challenge to accurately pinpoint its relationship to either the sunspot count in the group or the area. In contrast, as demonstrated in Figures 6 and 7, the X-band solar mapping likely provides a better picture of active regions as they evolve and helps to track their evolution across the solar disk, forewarning of intense solar eruptions.

6. Solar Synoptic Maps

6.1. Brightness Temperature Distribution

Apart from the daily radio maps of the Sun, displaying its brightness temperature distribution over a solar rotation is an efficient way to represent the full surface features of the Sun during a rotation, yielding a global view of emission structures. Moreover, it is a valuable tool for assessing the conditions of the emission characteristics in relationship to the solar magnetic field evolution. Figure 10 shows an example of a solar synoptic map, obtained using the continuous data from the 12-m telescope at 8647 MHz for the month of April 2022. This includes the full Carrington rotation #2256, spanning from 03 to 30 April 2022 and end

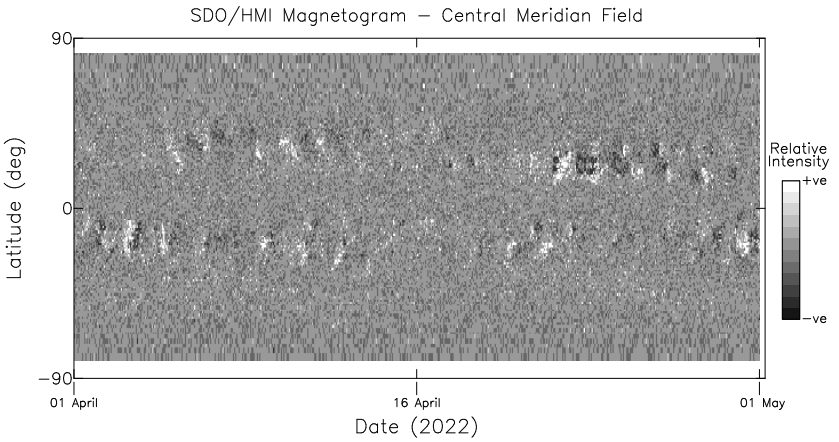

Figure 11. The synoptic map of the photospheric magnetic field generated using near-central-meridian magnetogram data from the HMI/SDO for the month of April 2022 is plotted in the same format as Figure 10.

part of the previous rotation. To construct the synoptic map, a central meridian cut of width ∼5 arcmin is taken from the daily radio images, covering from the south to the north poles. Since the spatial resolution of the 12-m telescope at X-band is ∼10 arcmin, the strip of ∼5 arcmin at the center of the Sun corresponds to the peak of the beam. The vertical central meridian strips are assembled horizontally in chronological order and deprojected to get a uniform latitudinal view of the solar features.

The synoptic map representation allows us to examine the temporal evolution of surface characteristics of the Sun. For example, in Figure 10, two bright regions, one in the southern hemisphere, centered around 03 April (due to the combination of active regions ARs#2978 and #2981, both of which developed to the complex β-γ configuration), and the other in the northern hemisphere, centered around 21 April 2022 (due the active regions ARs#2993 and #2994 of β-γ configuration) are evidently seen. Although both of them have a similar sort of magnetic configuration, the later active region's brightness temperature was much higher than that of the earlier one. This indicates that the small scale magnetic structures favorable in accelerating particles to high energy are likely present in the bright emitting region (e.g., Kumar, Manoharan, and Uddin 2010). Other interesting structures (or features) are the low emitting strips (i.e., <7000 K) extending from the north and south poles to mid latitudes, which are due to the small to large-size transient coronal holes (represented by red color code). Examples are at around 05 April and 22 April 2022. Consistently, the stability of the long lived low-emitting coronal holes in the high-latitude regions are brought out on the map. However, at the south and north edges of the map, the effect of the sky dilution can tend to reduce the temperature at a constant level and about 7-degree portion of the polar region edges are avoided while preparing the map. !in the map display. The bright emitting belt of about ±35° caused by the presence of sunspots (represented by the green color code) is apparent in the map. There are also a number of dark green features seen on

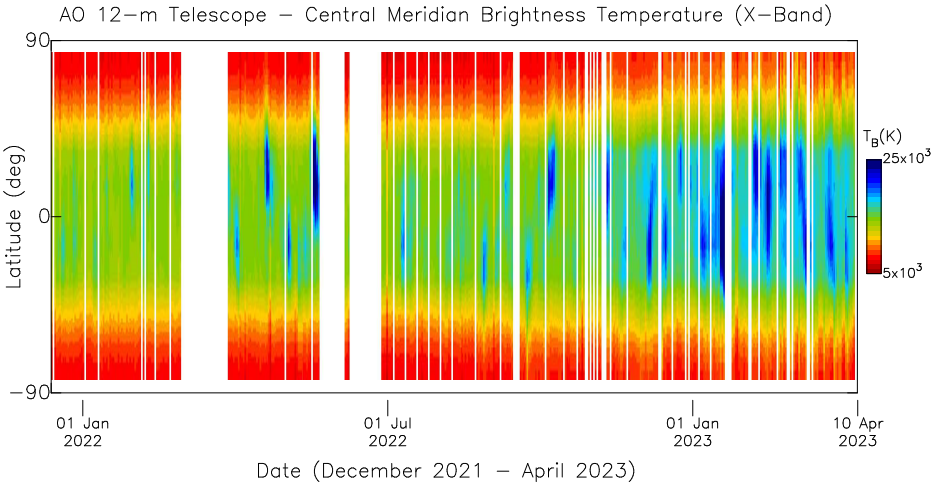

Figure 12. The heliographic latitudinal distribution of X-band brightness temperature observed by the Arecibo 12-m radio telescope as a function of the date. In the rising phase of the current solar cycle #25, around January 2022, the brightness around the equatorial closed-field region of the Sun was narrow in latitudinal spread compared to the brightness distribution observed in March – April 2023. The white patches represent observational gaps due to the telescope maintenance.

the equatorial belt, indicating the brightening of low-latitude sunspots. Due to the limited resolution of the 12-m telescope, the fine structures in the map have been smoothed to the beam size. Nevertheless, most of the large-scale features and low- and high-emitting regions are revealed.

6.2. The Photospheric Magnetic Field Distribution

The X-band brightness temperature distribution of the Sun has been compared with the magnetogram map of the observed photospheric magnetic field by HMI on board SDO. Figure 11 shows the synoptic map prepared with the near-central-meridian data from magnetograms acquired everyday around at ∼12 UT in the month of April 2022, which corresponds to the ascending phase of the current cycle #25 just after its minimum phase. The positive and negative polarities are respectively shown in white and black shades. At the initial phase of a solar cycle, sunspots appear at the high latitudes in the southern and northern hemispheres as is clearly revealed by two striking horizontal strips on the synoptic map. Moreover, the concentrated magnetic fields above two prominent active regions, corresponding to the bright emitting regions on the radio map (see Figure 10), can also be easily identified. Such a map is extremely useful to study the global distribution of solar features as a function of solar rotation.

7. Ascending Phase of Solar Cycle #25

7.1. Latitudinal Distribution of the Sun′s Brightness Temperature

The 12-m telescope observations covered a good portion of the ascending phase of the current solar cycle #25, between 13 December and 09 April 2023. More than 2000 solar images have been obtained. Since the data covered a large number of solar rotations, Carrington rotations from #2252 to #2268 (plus the beginning portion of rotation #2269; i.e., more than 17 rotations), the daily maps include the characteristics of repeating active regions, which lived for more than one solar rotation. In order to visualize the radio features of the Sun over these rotations, the same procedure used in preparing the radio synoptic map (see Figure 10) is employed and a central meridian strip of width ∼5 arcmin is taken from each day's image and the "*Latitude – Time*" plot of the brightness temperature is constructed as shown in Figure 12. This plot includes observations taken during the entire period of 13 December 2021 – 09 April 2023. In a broad sense, the "*Latitude – Time*" plot resembles the "*sunspot butterfly*" diagram and reveals the changes of the major large-scale magnetic and brightness structures and the development of activity occurring in the ascending phase of solar cycle #25. Despite several observational gaps, the brightness distribution shows a number of interesting features and the evidence of a steady increase in solar activity. For reference, the sunspot number and the strength of the smoothed polar magnetic fields are also displayed in Figure 13 with the help of data sets from the Wilcox Solar Observatory (http://wso.stanford.edu/) and the NASA/GSFC's OMNI database (http://omniweb.gsfc.nasa.gov/).

In Figure 12, the presence of an active region is identified with enhanced brightness temperature, >8000 K. Some of the active regions of large area (i.e., extended in longitude) have taken many days to cross the central meridian line and their signatures are wider along the time axis. The quiet Sun regions are at an average temperature of about 8000 K. In the case of a well-developed active region of complex magnetic configuration, a much higher brightness temperature is observed. For instance temperatures ≥13,000 K serve to identify active regions susceptible to intense flares and energetic Earth-directed CMEs leading to severe space-weather impacts. The notable point is that all the M-class flares were produced when the brightness temperature was ≥13,000 K, whereas X-class flares occurred close to the peak at ∼20,000 K (see Figures 5 and 6).

In Figure 12, the increase in the number of active regions in association with the sunspot count is shown by the number of bright emitting regions. The development of solar activity is also clearly indicated by the gradual increase in the latitudinal width of the brightness distribution as the sunspot number increases from mid-December 2021 to April 2023. In general, as the solar activity increases, the progressive shrinking of the low-density as well as low-emitting coronal holes towards the poles is observed (e.g., Manoharan 2012; Hathaway 2015, Hamada, Asikainen, and Mursula 2020). In the corresponding phase of solar cycle #25, the brightness temperature distribution is consistent with the structural change of the coronal holes in the polar regions respectively shown the gradual decrease in polar field strength at latitudes greater than 60 degrees (Figure 13) and the

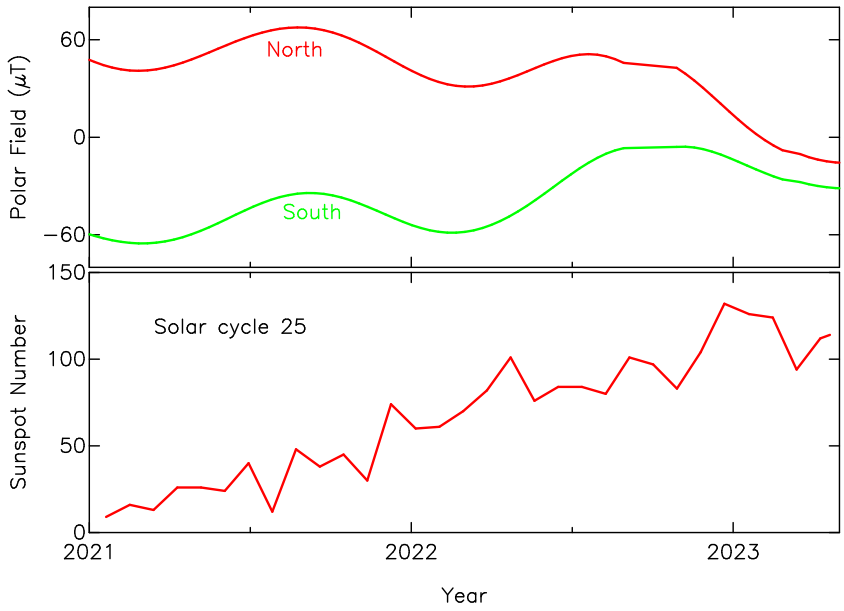

Figure 13. (Lower) The sunspot number, and (upper) the intensity of the polar magnetic field (red and green lines respectively for north and south polar regions), plotted as a function of the year. The increase of solar activity revealed by the sunspot count, as well as the gradual decrease of polar field strength, suggests a change from a near dipole magnetic configuration of the Sun to a complex structure when the activity increased (http://wso.stanford.edu/ and http://omniweb.gsfc.nasa.gov/).

density distribution inferred from the white-light coronagraph image (Figure 14). But, as discussed in Section 6.1, the sky dilution can add a constant reduction to the brightness temperature at the south and north edges of the map. The presence of mid- and low-latitude coronal holes at the central meridian of the Sun, shown by X-ray and EUV images of the Sun, is also observed as vertical low-emitting strips on the latitudinal distribution of Figure 12. The "Latitude – Time" plot, not only presents a clear picture of the development of solar activity, but also provides the three-dimensional view of radio emission at chromospheric heights in association with the solar surface features.

7.2. Density Evolution in the Near-Sun Region

The above results for brightness temperature distribution observed with the 12-m telescope are also consistent with the latitudinal distribution of Thomson-scattered brightness observed by the LASCO-C2 coronagraph on board the *Solar and Heliospheric Observatory* spacecraft (e.g., Brueckner et al. 1995; https://lasco-www.nrl.navy.mil/). Figure 14 shows the "*Latitude – Time*" image of the white light, which is associated with the density of free electrons, measured at 4 solar radii above the east limb of the Sun by the LASCO-C2 coronagraph for the period of the X-band plot shown in Figure 12 (e.g., Manoharan 2009; Thompson et al. 2011). The gradual increase in the latitude width of high density features,

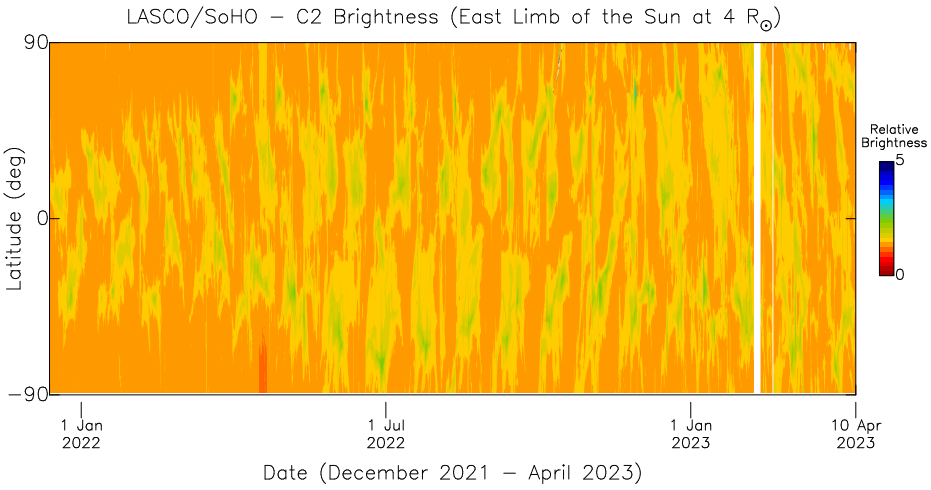

Figure 14. Heliographic latitudinal distribution of Thomson-scattered brightness observed at 4 solar radii by the LASCO-C2 coronagraph, as a function of the date. This plot covers the same period as Figure 12.

associated with closed-field active regions, is consistent with the distribution of X-band brightness temperature. Moreover, the decrease in the width of the low-density coronal hole regions at the poles are consistent with the brightness temperature distribution. Another remarkable feature seen in the LASCO plot is the low-density vertical patch near the south pole centered around 11 - 15 April 2022. This was associated with a large coronal hole located at the south pole of the Sun and extended from the pole to a latitude of about 50 degrees. The LASCO-C2 observed the low-density feature at the east limb of the Sun. As this coronal hole rotated to the center of the Sun in about 7 days, it was recorded by the 12-m telescope around 21 - 22 April 2022 (see Figure 12).

7.3. Radio Flux Density as a Function of Observing Frequency

The latitudinal manifest of the brightness temperature over about 17 solar rotations is apparent in Figure 12. The bright patches are regions of gyro-resonance (or gyro-synchrotron) emission, high magnetic field and significant plasma heating (i.e., due to high number density). This emission has a spectral peak in the range of 5 – 10 GHz (e.g, Nindos 2020; White and Kundu 1997) and it dominates the emission at frequencies, below 3 GHz (optically thick part of the solar atmosphere). It will be useful to compare the X-band temperature distribution with the time series analysis of radio flux measurements of the Sun at different wavelengths (e.g., in the meter to centimeter wavelength range). Such measurements include (i) background emission from the quiet Sun which does not vary with time (e.g., Kundu 1965)), (ii) the slowly varying component, caused by free-free thermal emission (e.g., White and Kundu 1997), and (iii) transient or sporadic emission caused by non-thermal electrons accelerated at flare and/or CME sites (e.g., Manoharan and Kundu 2003).

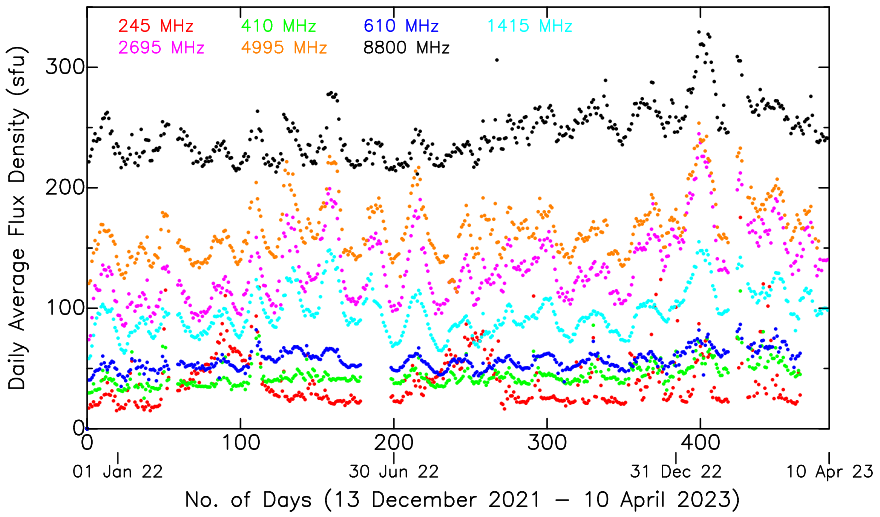

Figure 15. Daily average solar flux densities for the period between 13 December 2021 and 10 April 2023 at frequencies of 245, 410, 610, 1415, 2695, 4995, and 8800 MHz. The data sets are from the Learmonth Solar Observatory, which is one of the stations of the USAF Radio Solar Telescope Network (RSTN) (https://www.sws.bom.gov.au/WDC/).

Figure 15 shows the daily average solar flux densities observed in the frequency range of 245 – 8800 MHz by the Learmonth Solar Observatory, which is one of the stations of the Radio Solar Telescope Network (RSTN). The solar flux density is normally expressed in solar flux units (sfu) (1 sfu = 10^4 Jansky (Jy), where 1 Jy = 10^{-26} $\mathrm{Wm^{-2}\ Hz^{-1}}$). The solar radio flux data, recorded by four sites around the globe, are made available by the NOAA SWPC (https://www.ngdc.noaa.gov/stp/space-weather/solar-data/). In Figure 15, a gradual increase in the solar activity can been seen in most of the flux density profiles, between 13 December 2021 and 10 April 2023.

7.4. Radio Flux Density and Brightness Temperature

It will be effective to compare the solar flux density observed at 8.8 GHz at the Learmonth Solar Observatory (Figure 15) with the Arecibo daily average radio brightness temperature at the same frequency. This provides a relationship between the brightness temperature and solar flux density measured by two independent telescopes. Figure 16 (top panel) shows the daily average flux density measured at 8.8 GHz by the 2.4-m telescope at Learmonth Solar Observatory for the period between 13 December 2021 and 09 April 2023 (the flux-density profile at 8.8 GHz is reproduced from Figure 15). In the bottom panel of the figure, the daily average brightness temperature at 8.8 GHz from the Arecibo 12-m telescope is plotted. The detailed profiles from the two telescopes show one-to-one correlation. In particular, the overall trend of increasing intensity of the emission from the start of the profiles to the end, in association with the increasing solar activity, also shows the agreement between these two observations.

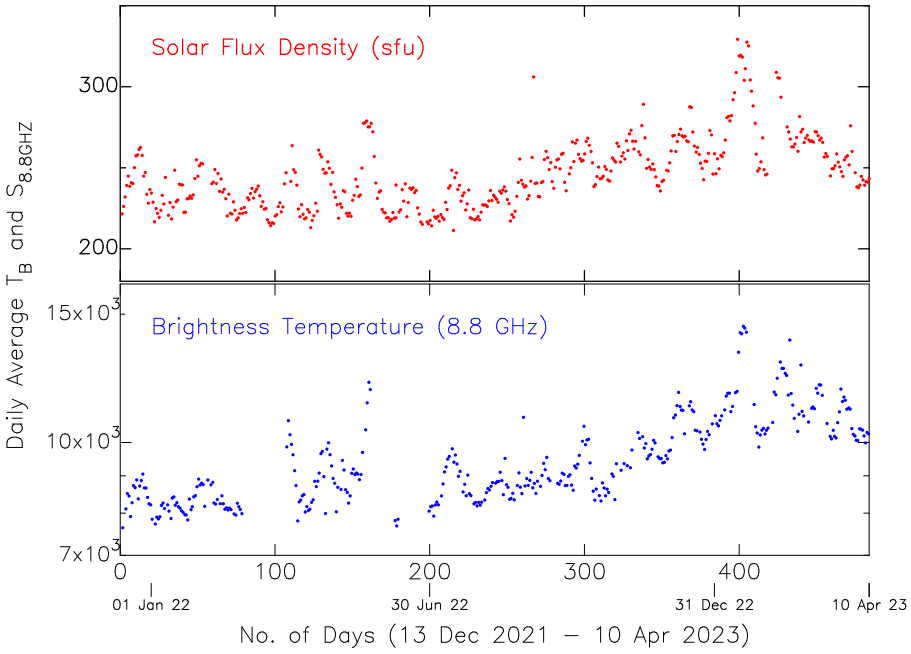

Figure 16. (Upper) Daily average solar radio flux density observed with the 2.4-m Learmonth Solar Observatory telescope, which is part of the RSTN network, at 8.8 GHz plotted between 13 December and 09 April 2023. (Lower) Daily average brightness temperature observed at 8.8 GHz with the Arecibo 12-m telescope. The variations seen in the radio flux density profile agree well with those seen in the average Arecibo brightness temperature. The overall increasing trend seen in both profiles is in agreement with the increasing solar activity from the start to end of the data stretch.

Figure 17 shows the correlation plot between the daily average flux density at Learmonth and the daily average Arecibo brightness temperature at 8.8 GHz. (In this plot, at brightness temperatures >10000 K, the flux densities tend to deviate moderately towards lower values, which may require a through investigation of the linearity of the flux density measurements at high levels of activity.) For a given brightness temperature, mean-to-peak fluctuations of $\leq$10% in the radio flux densities are observed. An overall linear correlation coefficient of 81% between the two measured parameters indicates the close agreement between them. This correlation was further checked and confirmed, in the Rayleigh-Jeans approximation to Planck′s radiation law, by converting the observed X-band brightness temperature to flux density over the disk of the Sun. In this phase of solar cycle #25, the average flux density at 8.8 GHz was ∼245 sfu. The daily ratios between the brightness temperature and the flux density at 8.8 GHz, ($T_B/S_{8.8GHz}$), vary between ∼28 and ∼50 and have an average value of 38.2 K/sfu.

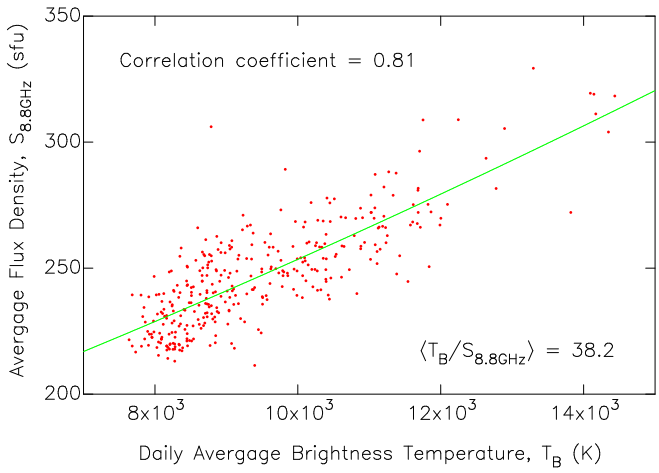

Figure 17. The correlation plot between the daily average solar flux density measurements from the Learmonth Solar Observatory (RSTN) and the brightness temperature estimates from the 12-m telescope at 8.8 GHz. The linear correlation coefficient between these two parameters is 0.81. The average ratio between the brightness temperature and the flux density is 38.2 K/sfu.

8. Concluding Remarks

In this paper, we present X-band solar mapping observations made with the Arecibo 12-m radio telescope in the frequency range of 8.1 – 9.2 GHz. These observations have revealed the highly complex and variable brightness distribution of solar features over several solar rotations of the current solar cycle #25, covering a fair portion of the ascending phase between 13 December 2021 and 09 April 2023. The solar maps have been used to locate and track active regions of space-weather importance. The radio signatures of an active region in the frequency range of 8 – 9 GHz provide a powerful diagnostic of the gyro-synchrotron radiation from high-energy electrons trapped in small-scale magnetic field loops (e.g., Nindos 2020) and the temporal brightness temperature changes of active regions have been compared with their area and magnetic configuration. Although a correlating tendency has been observed between the brightness temperature and the area of the active region, (also with the number of sunspots within it), understanding the differences in the formation, development, and decay of an active region in terms of its area and/or magnetic configuration alone poses a great challenge. Thus, a given area of an active group, (or the number of spots within it), may not be a precise parameter when deciding on the actual capacity of an eruption site. The results of the present study demonstrates that the X-band solar mapping provides an improved picture of the formation location of an active region and helps to accurately track its evolution across the solar disk, forewarning of intense solar eruptions leading to severe space-weather consequences.

Additionally, the "Latitude – Time" plot over several solar rotations provides the evolution of quiet regions on the Sun, coronal holes, and eruptive sites. This also provides the three-dimensional picture of radio emission (i) above sunspots, where the magnetic field is stronger, but less divergent, (ii) high- and mid-latitude coronal holes of largely unipolar and open field regions, and (iii) large-scale emitting structures, which can be linked to the flux emergence rate from regions below the photosphere. The present analysis emphasizes the importance of the long-term monitoring of the Sun at X-band for understanding the complex three-dimensional evolution of solar features as a function of solar activity. The agreement obtained between the daily radio flux density and brightness temperature data provides a typical scaling factor involved. However, this has to be further thoroughly checked for slowly varying emission and sporadic bursts caused by flares and CMEs with improved spatial resolution measurements.

During the X-band solar mapping observations, several CME events were also detected. These observations are useful towards understanding hot magnetized plasma conditions at the initial stages of CMEs at the chromospheric height. For academic interest, we also tracked a few active regions and recorded the brightness temperatures at the high temporal resolution. Results of the CME-event study and emission profile analysis will be presented elsewhere.

The 12-m radio telescope is currently being upgraded with a wideband, 2.3 – 14 GHz, cooled front-end system, which will considerably enhance its sensitivity, as well as its frequency coverage. Since the new receiver also allows measurement of full-Stokes parameters, its extended bandwidth will provide highly accurate temporal measurements of polarization and dynamic spectra of the solar emission. This will be valuable for studying the evolution of the magnetic-field configurations and plasma conditions in the magnetic current sheets of solar eruptions, which are essentially required for understanding the origin of space-weather events. Moreover, the mapping of the Sun over a wide frequency band will also provide the temporal and spatial evolution of the eruptive active regions at different layers between the photosphere and the lower corona.

In addition, the upgraded 12-m system will allow interplanetary scintillation (IPS) observations of compact background radio sources that can probe the ambient solar wind and structures within propagating CMEs in the three-dimensional inner heliosphere, for regions inaccessible to spacecraft, between the solar wind acceleration region and to about the middle Sun-Earth distance (∼10 – 100 solar radii) (e.g., Manoharan 2010). Indeed the wide bandwidth made available will allow us to probe solar-wind density structure of different scale sizes, *i.e.*, Fresnel radii, which are useful towards understanding the plasma properties associated with propagating space-weather events (e.g., Cohen and Gundermann 1969; Manoharan 1993). A set of solar observations at high- and low-radio frequencies respectively with the Arecibo 12-m radio telescope and the Arecibo Callisto Radio Spectrometer (https://www.e-callisto.org/), combined with IPS measurements, will be an asset for a detailed understanding of space-weather events in the Sun-Earth space.

Acknowledgements The Arecibo Observatory is operated by the University of Central Florida under a cooperative agreement with the National Science Foundation (AST-1822073), and in alliance with Universidad Ana G. Méndez and Yang Enterprises, Inc. PKM wishes to

thank Tapasi Ghosh for the numerous useful discussions and suggestions during the stages of analysis and the preparation of the manuscript. We acknowledge the EUV data from the UVE and images from the AIA and HMI on board the Solar Dynamics Observatory. The X-ray data sets have been obtained from the Geostationary Operational Environmental Satellite (GOES-16). We also acknowledge OMNIdata of NASA/GSFC's Space Physics Data Facility. The Wilcox Solar Observatory provided the source surface magnetic field data. The SOHO/LASCO is a project of international cooperation between ESA and NASA. We are grateful to the Learmonth Solar Observatory, one of the stations of the Radio Solar Telescope Network (RSTN), for the provision of the solar flux density data.

References

Avrett, E.H., Loeser, R.: 2008, Models of the Solar Chromosphere and Transition Region from SUMER and HRTS Observations: Formation of the Extreme-Ultraviolet Spectrum of Hydrogen, Carbon, and Oxygen. *The Astrophysical Journal Supplement Series* **175**, 229. DOI. ADS.

Bastian, T.S., Benz, A.O., Gary, D.E.: 1998, Radio Emission from Solar Flares. *Annual Review of Astronomy and Astrophysics* **36**, 131. DOI. ADS.

Brueckner, G.E., Howard, R.A., Koomen, M.J., Korendyke, C.M., Michels, D.J., Moses, J.D., Socker, D.G., Dere, K.P., Lamy, P.L., Llebaria, A., Bout, M.V., Schwenn, R., Simnett, G.M., Bedford, D.K., Eyles, C.J.: 1995, The Large Angle Spectroscopic Coronagraph (LASCO). *Solar Phys.* **162**, 357. DOI. ADS.

Cohen, M.H., Gundermann, E.J.: 1969, Interplanetary Scintillations.IV. Observations Near the Sun. *Astrophys. J.* **155**, 645. DOI. ADS.

Dabrowski, B.P., Benz, A.O.: 2009, Correlation between decimetric radio emission and hard X-rays in solar flares. *Astron. Astrophys.* **504**, 565. DOI. ADS.

Fleishman, G.D., Nita, G.M., Chen, B., Yu, S., Gary, D.E.: 2022, Solar flare accelerates nearly all electrons in a large coronal volume. *Nature* **606**, 674. DOI. ADS.

Gary, D.E., Bastian, T.S., Chen, B., Fleishman, G.D., Glesener, L.: 2018, Radio Observations of Solar Flares. In: Murphy, E. (ed.) *Science with a Next Generation Very Large Array*, *Astronomical Society of the Pacific Conference Series* **517**, 99. ADS.

Hale, G.E., Ellerman, F., Nicholson, S.B., Joy, A.H.: 1919, The Magnetic Polarity of Sun-Spots. *Astrophys. J.* **49**, 153. DOI. ADS.

Hamada, A., Asikainen, T., Mursula, K.: 2020, New Homogeneous Dataset of Solar EUV Synoptic Maps from SOHO/EIT and SDO/AIA. *Solar Phys.* **295**, 2. DOI. ADS.

Hathaway, D.H.: 2015, The Solar Cycle. *Living Reviews in Solar Physics* **12**, 4. DOI. ADS.

Jaeggli, S.A., Norton, A.A.: 2016, The Magnetic Classification of Solar Active Regions 1992-2015. *Astrophys. J. Lett.* **820**, L11. DOI. ADS.

Krucker, S., Battaglia, M., Cargill, P.J., Fletcher, L., Hudson, H.S., MacKinnon, A.L., Masuda, S., Sui, L., Tomczak, M., Veronig, A.L., Vlahos, L., White, S.M.: 2008, Hard X-ray emission from the solar corona. *Astron. Astrophys. Rev.* **16**, 155. DOI. ADS.

Kumar, P., Manoharan, P.K., Uddin, W.: 2010, Evolution of Solar Magnetic Field and Associated Multiwavelength Phenomena: Flare Events on 2003 November 20. *The Astrophysical Journal* **710**, 1195. DOI. https://dx.doi.org/10.1088/0004-637X/710/2/1195.

Kundu, M.R.: 1965, *Solar Radio Astronomy*, Interscience Publishers, John Wiley & Sons, New York. ADS.

Künzel, H.: 1965, Zur Klassifikation von Sonnenfleckengruppen. *Astronomische Nachrichten* **288**, 177. ADS.

Lemen, J.R., Title, A.M., Akin, D.J., Boerner, P.F., Chou, C., Drake, J.F., Duncan, D.W., Edwards, C.G., Friedlaender, F.M., Heyman, G.F., Hurlburt, N.E., Katz, N.L., Kushner, G.D., Levay, M., Lindgren, R.W., Mathur, D.P., McFeaters, E.L., Mitchell, S., Rehse, R.A., Schrijver, C.J., Springer, L.A., Stern, R.A., Tarbell, T.D., Wuelser, J.-P., Wolfson, C.J., Yanari, C., Bookbinder, J.A., Cheimets, P.N., Caldwell, D., Deluca, E.E., Gates, R., Golub, L., Park, S., Podgorski, W.A., Bush, R.I., Scherrer, P.H., Gummin, M.A., Smith, P., Auker, G., Jerram, P., Pool, P., Soufli, R., Windt, D.L., Beardsley, S., Clapp, M., Lang, J., Waltham, N.: 2012, The Atmospheric Imaging Assembly (AIA) on the Solar Dynamics Observatory (SDO). *Solar Phys.* **275**, 17. DOI. ADS.

Manoharan, P.K.: 1993, Three-Dimensional Structure of the Solar Wind - Variation of Density with the Solar Cycle. *Solar Phys.* **148**, 153. DOI. ADS.

Manoharan, P.K.: 2009, Peculiar Current Solar-Minimum Structure of the Heliosphere. *Highlights of Astronomy* **15**, 484. DOI. ADS.

Manoharan, P.K.: 2010, Ooty Interplanetary Scintillation - Remote-Sensing Observations and Analysis of Coronal Mass Ejections in the Heliosphere. *Solar Phys.* **265**, 137. DOI. ADS.

Manoharan, P.K.: 2012, Three-dimensional Evolution of Solar Wind during Solar Cycles 22-24. *The Astrophysical Journal* **751**, 128. DOI. https://dx.doi.org/10.1088/0004-637X/751/2/128.

Manoharan, P.K., Kundu, M.R.: 2003, Coronal Structure of a Flaring Region and Associated Coronal Mass Ejection. *The Astrophysical Journal* **592**, 597. DOI. https://dx.doi.org/10.1086/375700.

Manoharan, P.K., Salter, C.J., Brum, C.M., White, S.M., Perillat, P., Santoni, A., Fernandez, F., Ghosh, T., Perera, B., Venkataraman, A.: 2022, Regular Solar Radio Imaging at Arecibo: Space Weather Perspective of Evolution of Active Regions. *arXiv e-prints*, arXiv:2211.04472. ADS.

Manoharan, P.K., Salter, C., Garnett Marques Brum, C., White, S., Perillat, P., Santoni, A., Fernandez, F., Ghosh, T., Perera, B., Venkataraman, A.: 2023, Regular Solar Radio Imaging at Arecibo: Space Weather Perspective of Evolution of Active Regions. In: *American Astronomical Society Meeting Abstracts*, *American Astronomical Society Meeting Abstracts* **55**, 226.05. ADS.

Nindos, A.: 2020, Incoherent Solar Radio Emission. *Frontiers in Astronomy and Space Sciences* **7**, 57. DOI. ADS.

Nita, G.M., Gary, D.E., Lee, J.: 2004, Statistical Study of Two Years of Solar Flare Radio Spectra Obtained with the Owens Valley Solar Array. *Astrophys. J.* **605**, 528. DOI. ADS.

Perera, B., Perillat, P., Fernandez, F., Manoharan, P., Roshi, A., Salter, C., Smith, A., Vaddi, S., McGilvray, A.: 2022, Detection of a bright burst from FRB 20220912A at 2.3 GHz with the Arecibo 12-m telescope. *The Astronomer's Telegram* **15734**, 1. ADS.

Perera, B., Perillat, P., Doskoch, G., Manoharan, P., McLaughlin, M.: 2023, Daily monitoring of pulsars with the Arecibo 12-m telescope: the current and future. In: *American Astronomical Society Meeting Abstracts*, *American Astronomical Society Meeting Abstracts* **55**, 304.10. ADS.

Pesnell, W.D., Thompson, B.J., Chamberlin, P.C.: 2012, The Solar Dynamics Observatory (SDO). *Solar Phys.* **275**, 3. DOI. ADS.

Priest, E.R., Forbes, T.G.: 2002, The magnetic nature of solar flares. *Astron. Astrophys. Rev.* **10**, 313. DOI. ADS.

Scherrer, P.H., Schou, J., Bush, R.I., Kosovichev, A.G., Bogart, R.S., Hoeksema, J.T., Liu, Y., Duvall, T.L., Zhao, J., Title, A.M., Schrijver, C.J., Tarbell, T.D., Tomczyk, S.: 2012, The Helioseismic and Magnetic Imager (HMI) Investigation for the Solar Dynamics Observatory (SDO). *Solar Phys.* **275**, 207. DOI. ADS.

Shibasaki, K., Alissandrakis, C.E., Pohjolainen, S.: 2011, Radio Emission of the Quiet Sun and Active Regions (Invited Review). *Solar Phys.* **273**, 309. DOI. ADS.

Thompson, B.J., Gibson, S.E., Schroeder, P.C., Webb, D.F., Arge, C.N., Bisi, M.M., de Toma, G., Emery, B.A., Galvin, A.B., Haber, D.A., Jackson, B.V., Jensen, E.A., Leamon, R.J., Lei, J., Manoharan, P.K., Mays, M.L., McIntosh, P.S., Petrie, G.J.D., Plunkett, S.P., Qian, L., Riley, P., Suess, S.T., Tokumaru, M., Welsch, B.T., Woods, T.N.: 2011, A Snapshot of the Sun Near Solar Minimum: The Whole Heliosphere Interval. *Solar Phys.* **274**, 29. DOI. ADS.

White, S.M.: 1999, Radio Versus EUV/X-Ray Observations of the Solar Atmosphere. *Solar Phys.* **190**, 309. DOI. ADS.

White, S.M., Kundu, M.R.: 1997, Radio Observations of Gyroresonance Emission from Coronal Magnetic Fields. *Solar Physics* **174**, 31. DOI. ADS.

White, S.M., Benz, A.O., Christe, S., Fárník, F., Kundu, M.R., Mann, G., Ning, Z., Raulin, J.-P., Silva-Válio, A.V.R., Saint-Hilaire, P., Vilmer, N., Warmuth, A.: 2011, The Relationship Between Solar Radio and Hard X-ray Emission. *Space Sci. Rev.* **159**, 225. DOI. ADS.

Woods, T.N., Eparvier, F.G., Hock, R., Jones, A.R., Woodraska, D., Judge, D., Didkovsky, L., Lean, J., Mariska, J., Warren, H., McMullin, D., Chamberlin, P., Berthiaume, G., Bailey, S., Fuller-Rowell, T., Sojka, J., Tobiska, W.K., Viereck, R.: 2012, Extreme Ultraviolet Variability Experiment (EVE) on the Solar Dynamics Observatory (SDO): Overview of Science Objectives, Instrument Design, Data Products, and Model Developments. *Solar Phys.* **275**, 115. DOI. ADS.

Yashiro, S., Gopalswamy, N., Akiyama, S., Michalek, G., Howard, R.A.: 2005, Visibility of coronal mass ejections as a function of flare location and intensity. *Journal of Geophysical Research (Space Physics)* **110**, A12S05. DOI. ADS.

Zhang, J., White, S.M., Kundu, M.R.: 1998, The Height Structure of the Solar Atmosphere from the Extreme-Ultraviolet Perspective. *The Astrophysical Journal* **504**, L127. DOI. https://dx.doi.org/10.1086/311587.